Dynamics of anchored oscillating nanomenisci

Caroline Mortagne,[1,2] Kevin Lippera,[1,3] Philippe Tordjeman,[2]
Michael Benzaquen,[3] and Thierry Ondarçuhu[1,*]

[1]*CEMES-CNRS, UPR 8011, 29 rue Jeanne Marvig, 31055 Toulouse Cedex 4, France*
[2]*IMFT-Université de Toulouse, CNRS-INPT-UPS, UMR 5502,*
1 allée du Professeur Camille Soula, 31400 Toulouse, France
[3]*LadHyX-UMR CNRS 7646, École Polytechnique, Boulevard des Maréchaux, 91120 Palaiseau, France*

We present a self-contained study of the dynamics of oscillating nanomenisci anchored on nanometric topographical defects around a cylindrical nanofiber with a radius below 100 nm. Using frequency-modulation atomic force microscopy (FM-AFM), we show that the friction coefficient surges as the contact angle is decreased. We propose a theoretical model within the lubrication approximation that reproduces the experimental data and provides a comprehensive description of the dynamics of the nanomeniscus. The dissipation pattern in the vicinity of the contact line and the anchoring properties are discussed as a function of liquid and surface properties in addition to the forcing conditions.

I. INTRODUCTION

The study of liquid dynamics in the close vicinity of the contact line is fundamental to understanding the physics of wetting [1,2]. The strong confinement inherent to this region leads, in the case of a moving contact line, to a divergence of the energy dissipation. This singularity can be released by the introduction of microscopic models based on long-range interactions, wall slippage, or diffuse interface [3], which are still difficult to determine experimentally. In most cases, the spreading is also controlled by the pinning of the contact line on surface defects [4,5]. For nanometric defects, the intensity and localization of the viscous energy dissipation is crucial to understanding the wetting dynamics. The aim of this paper is to study the hydrodynamics of a nanomeniscus anchored on nanometric topographic defects and subjected to an external periodic forcing. This configuration allows one to investigate the viscous dissipation in a meniscus down to the very close vicinity of the fixed contact line and to assess the dynamics of the pinning of nanometric defects. In addition to being an important step towards the elucidation of the wetting dynamics on rough surfaces, this issue is relevant for vibrated droplets or bubbles [6] and for the reflection of capillary waves on a solid wall [7].

Atomic force microscopy (AFM) has proven to be a unique tool to carry out measurements on liquids down to the nanometer scale: liquid structuration [8] or slippage [9] at solid interfaces was evidenced, while the use of specific tips fitted with either micro- or nanocylinders allowed quantitative measurements in viscous boundary layers [10] and at the contact line [11]. In this study, we have developed an AFM experiment based on the frequency modulation mode (FM-AFM) to monitor, simultaneously, the mean force and the energy dissipation experienced by an anchored nanomeniscus. Artificial defects with adjustable size are deposited on cylindrical fibers (radius below 100 nm) to control the pinning of the contact line and the meniscus stretching during the oscillation. The experiments are analyzed in the frame of a nanohydrodynamics model based on the lubrication approximation. Interestingly, the meniscus oscillation does not lead to any stress divergence at the contact line allowing a full resolution without the use of cutoff lengths in contrast with the case of a moving contact line. This study thus provides a comprehensive description of
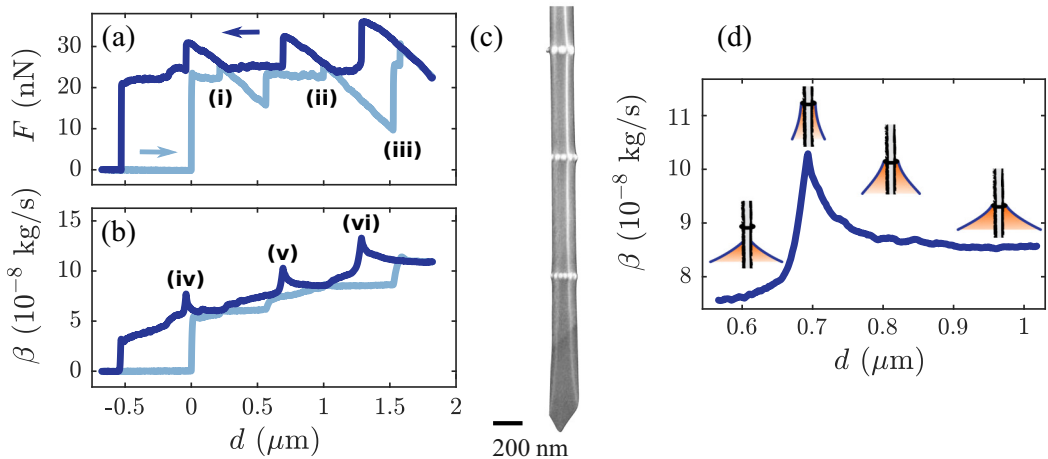
---

*ondar@cemes.fr

FIG. 1. FM-AFM spectroscopy curves performed on a 3EG liquid drop. (a) Force F and (b) friction coefficient β as a function of the immersion depth d. (c) SEM image of the 3.2 μm long and 170 nm diameter probe, covered by three platinum rings of thicknesses $r_0 = 10$, 15, and 40 nm, from bottom to top. (d) Zoom on the friction coefficient curve on the second defect with sketches of the meniscus.

dissipation mechanisms in highly confined menisci and an estimate of the critical depinning contact angle for nanometric defects.

II. EXPERIMENTAL METHODS

The fibers used in the experimental study were carved with a dual beam FIB (1540 XB Cross Beam, Zeiss) from conventional silicon AFM probes (OLTESPA, Bruker). Using a beam of Ga ions, a 2 to 3 μm long cylinder of radius $R \sim 80$ nm is milled at the end of a classical AFM tip. An ELPHY MultiBeam (Raith) device allows to manufacture nanometric spots of platinum by electron beam induced deposition (EBID) in order to create ring defect of controlled thickness around the cylinders (see Supplemental Material [12]). An example of a homemade cylinder with three annular rings is displayed in Fig. 1(d). The liquids used are ethylene glycol (1EG), diethylene glycol (2EG), triethylene glycol (3EG), and an ionic liquid, namely, 1-ethyl-3-methylimidazolium tetrafluoroborate. The liquids have a low volatility at room temperature. Their dynamic viscosities are $\eta = 19.5$, 34.5, 46.5, and 44 mPa $\cdot$ s, and their surface tensions are $\gamma = 49.5$, 49.5, 48, and 56 mN $\cdot$ m^{-1} at 20°, respectively. As surface conditions play a crucial role in wetting, measurements are made before and after a 5 min UV/O$_3$ treatment aimed at removing contaminants and making the surface more hydrophilic [13].

Using a PicoForce AFM (Bruker), the tips are dipped in and withdrawn from a millimetric liquid drop deposited on a silicon substrate. Prior to any experiment series, the cantilever quality factor Q and deflection sensitivity are measured, and its spring constant k is determined using standard calibration technique[14]. The experiments are performed in frequency modulation (FM-AFM) mode using a phase-lock loop device (HF2LI, Zurich Instrument) which oscillates the cantilever at its resonance frequency f. A proportional-integral-derivative controller is used to adjust the excitation signal A_{ex} in order to maintain the tip oscillation amplitude A constant. The excitation signal A_{ex} is therefore a direct indication of the system dissipation. In particular, it is linearly related to the friction coefficient of the interaction through $\beta = \beta_0 (A_{\text{ex}}/A_{\text{ex},0} - 1)$, where $A_{\text{ex},0}$ and $\beta_0 = k/(\omega_0 Q)$ are, respectively, the excitation signal and the friction coefficient of the free system in air, measured far from the liquid interface [15]. We used cantilevers with quality factor $Q \sim 200$ high enough to ensure that the resonant frequency is related to the natural angular frequency through $\omega_0 = 2\pi f$. We showed recently that this procedure, and the appropriate calibration used, gives quantitative

measurements of dissipation in the viscous layer around the tip [10]. In the present case, it allows us to monitor, during the whole process, both the capillary force F and the friction coefficient β, which are related to the shape of the meniscus and to the viscous dissipation, respectively. Note that both values are obtained with a 20% accuracy mainly coming from the uncertainty in the determination of k.

III. RESULTS

Figure 1 shows the results of a typical experiment performed on a 3EG drop. The measured force F [Fig. 1(a)] and friction coefficient β [Fig. 1(b)] are plotted as a function of the immersion depth d for a ramp of $2.5\,\mu$m. The cylinder is dipped in (light blue curves) and withdrawn (dark blue curves) from the liquid bath at $2.5\,\mu$m $\cdot$ s^{-1}. The tip oscillates at its resonance frequency (66 820 Hz in air) with an amplitude of 6 nm. The cantilever stiffness is $k = 1.5\,$N $\cdot$ m^{-1}, soft enough to perform deflection measurements while being adapted for the dynamic mode. The force curve can be interpreted using the expression of the capillary force [16]: $F = 2\pi R\gamma \cos\bar{\theta}$, where R is the fiber radius and $\bar{\theta}$ is the mean contact angle during the oscillation. After the meniscus formation at $d = 0$, and until the contact line anchors on the first ring [at reference (i)] F and $\bar{\theta}$ remain constant, consistent with Refs. [16–18]. A small jump of the force is observed when the contact line reaches a platinum ring on reference points (i), (ii), or (iii). Once the meniscus is pinned, the contact angle increases as the cylinder goes deeper into the liquid, leading to a decrease of the force F. Conversely, the withdrawal leads to a decrease of $\bar{\theta}$ and an increase of the force F on the left of (i), (ii), and (iii). Hence, each ring induces two hysteresis cycles characteristic of strong topographic defects [4].

Different contributions to the probe-liquid system account for the friction coefficient behavior. The global increase of β with d observed on Fig. 1(b) results from the contribution of the viscous layer around the tip which is proportional to the immersion depth [10]. At withdrawal, β increases dramatically when the probe reaches the reference points (iv), (v), and (vi) of Fig. 1(b). In those regions, the force curve indicates that the meniscus is pinned on a defect. The dissipation growth is therefore attributed to the decrease of the contact angle before depinning as schematized on the zoom on the friction coefficient curve [Fig. 1(c)]. This large effect can be qualitatively understood considering that small contact angles—corresponding to reduced film thickness—generate strong velocity gradients in the meniscus and thus a large dissipation. Note that a similar behavior is observed on a moving contact line for which the friction coefficient also displays a strong dependance upon the contact angle $\beta \sim 1/\bar{\theta}$ [1].

IV. THEORETICAL MODEL

In order to account for the experimental results, we developed a theoretical model for the oscillation of a liquid meniscus in cylindrical geometry (see the Supplemental Material [12]). We consider the problem in the frame of reference attached to the cylinder (see Fig. 2). The flow induced by the interface motion leads to a friction coefficient β_{men}. The latter is related to the mean energy loss $\mathcal{P}$ during an oscillation cycle, through $\mathcal{P} = \beta_{\mathrm{men}}(A\omega)^2/2$ [19]. Since the capillary number is small (see Ref. [20]) we may safely state that viscous effects do not affect the shape of the liquid interface. Therefore, the meniscus profile is solution of the Laplace equation resulting from the balance between capillary and hydrostatic pressures, which in turn yields the well-known catenary shape [21–23]:

$$h = (R + r_0)\cos\theta \cosh\left[\frac{z}{(R + r_0)\cos\theta} - \ln(\zeta)\right] \qquad (1)$$

were $\zeta = \cos\theta/(1 + \sin\theta)$. The meniscus height Z_0 is given, in the limit of small contact angles, by

$$Z_0 = (R + r_0)\cos\theta\left[\ln\left(\frac{4\,l_c}{R + r_0}\right) - \gamma_E\right] \qquad (2)$$
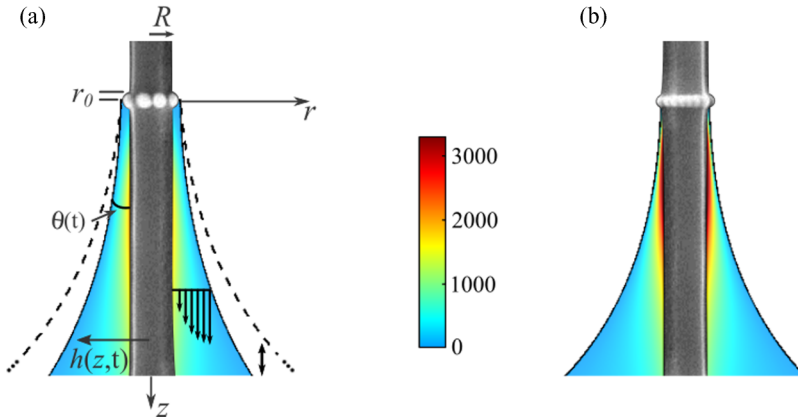
FIG. 2. (a) Oscillating meniscus anchored on a defect, displayed in the frame of reference of the fiber. The velocity profile (black arrows) is calculated from Eq. (4). The stress field $\eta \partial_r v$ (color gradient) is computed for $R = 100$ nm, $r_0 = 40$ nm, $l_c = 2$ mm, $A = 10$ nm, $f = 65$ kHz, $\bar{\theta} = \theta_{\mathrm{crit}} = 6.73°$, and $\eta = 30$ mPa $\cdot$ s. Color bar in Pa. (b) Same with $r_0 = 10$ nm and $\bar{\theta} = \theta_{\mathrm{crit}} = 7.5°$.

with $\gamma_E \simeq 0.577$ the Euler constant and l_c the capillary length. Since $Z_0(t)$ oscillates around its mean position as $Z_0[\theta(t)] = Z_0(\bar{\theta}) + A\cos(\omega t)$, we can derive the temporal evolution of the contact angle:

$$\cos\theta(t) = \cos\bar{\theta} + \frac{A\cos(\omega t)}{(R + r_0)\left[\ln\left(\frac{4l_c}{R+r_0}\right) - \gamma_E\right]}. \tag{3}$$

Note that our model is meant to deal with positive contact angles only, even if the defect thickness could in principle allow slightly negative ones. This defines a critical contact angle θ_{crit} related to the minimum value of $\bar{\theta}$ allowed by the model. One has $\cos\theta_{\mathrm{crit}} = 1 - A/((R + r_0)\{\ln[4\,l_c/(R + r_0)] - \gamma_E\})$. This critical depinning angle on an ideally strong defect increases with respect to A and decreases with respect to $R + r_0$. The interface motion being known, the velocity field is derived using the Stokes equation. Indeed, gravity and inertia can be safely neglected (Re $\sim 10^{-8}$ and $l_c \simeq 2$ mm). Moreover, the viscous diffusion time scale $\tau_v = R^2/\nu$ is much smaller than the oscillation period ($\tau_v f \sim 10^{-7}$), such that the Stokes equation reduces to the simplest steady Stokes equation. Using the lubrication approximation, we have finally $\partial_z P = \eta \Delta_r v$ where P is the hydrodynamic pressure and v is the velocity component in the z direction. Finally, combining the mass conservation equation, $\partial_t(\pi h^2) + \partial_z q = 0$, where q is the local flow rate through a liquid section of normal z, the no-slip (at $r = R$), and free interface (at $r = h$) boundary conditions yields the velocity profile:

$$v(r,z,t) = \frac{2[R^2 + 2\,h^2\,\ln(r/R) - r^2]\int_0^z du\,\partial_t(h^2)}{R^4 + 3\,h^4 - 4\,h^2\,R^2 - 4\,h^4\ln(h/R)}. \tag{4}$$

From Eq. (4) we derive the expression of β_{men}:

$$\beta_{\mathrm{men}}(\bar{\theta}) = \left\langle \frac{4\pi\eta}{A^2\omega^2} \int_0^{Z_0} \int_R^h (\partial_r v)^2 r\,dr\,dz \right\rangle_t, \tag{5}$$

where $\langle\,\rangle_t$, designates the temporal average over an oscillation cycle (see the Supplemental Material [12]). Figure 2 displays an example of viscous stress field (color gradient) and velocity profile (vertical dark arrows) inside a nanomeniscus. The latter are computed from Eqs. (1), (3), and (4) for a fiber of radius $R = 85$ nm and a defect with $r_0 = 10$ nm, for typical operating conditions ($f = 65$ kHz and $A = 10$ nm). We observe that the stress is essentially localized at the fiber wall and is at maximum at a distance of the order of R beneath the contact line. Interestingly, the
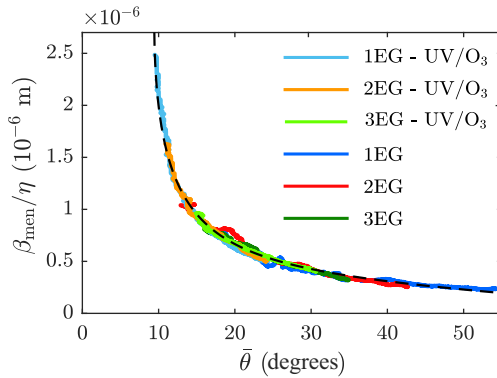
DYNAMICS OF ANCHORED OSCILLATING NANOMENISCI

FIG. 3. Normalized friction coefficient $\beta_{\mathrm{men}}/\eta$ plotted as a function of $\bar{\theta}$ [see Eq. (5)]. The dashed line signifies the theoretical model, and the experimental dotted curves are performed over all the studied liquids, before and after UV/O$_3$ treatment, with $R = 85\,\mathrm{nm}$, $A = 18\,\mathrm{nm}$, and $r_0 = 40\,\mathrm{nm}$. The values of the free parameters used are $\theta_{\mathrm{break}} = 18.5°$, $12.6°$, $15.1°$, $9.5°$, $10.9°$ and $14.9°$ and $\beta_{\mathrm{bottom}}/\eta R = 8.7$, 4.5, 10.2, 8.9, 13.2, 9.1 for 1EG, 2EG and 3EG, before and after UV/O$_3$ treatment, respectively.

meniscus oscillation does not lead to any stress singularity at the contact line. It does not require the introduction of a slippage in the vicinity of the (moving) contact line as in the case of wetting dynamics [24,25]. We therefore used the standard no-slip boundary condition, validated by the molecular scale values of slip lengths measured on hydrophilic surfaces [26]. The viscous stress maps also allow one to check *a posteriori* the interface profile hypothesis. The local capillary number is $\mathrm{Ca}_{\mathrm{local}} = \eta\partial_z v/\Delta P$ where $\Delta P \simeq \gamma/R - \gamma/(R + A) \simeq A\gamma/R^2$. Taking a maximum value of $\eta\partial_z v = 3000\,\mathrm{Pa}$ obtained for 10 nm defects [see Fig. 2(b)] we find that $\mathrm{Ca} \leqslant 5 \times 10^{-2}$, thus validating the hypothesis. The fact that the viscous stress strongly decays when z becomes of the order of a few probe radii also strengthens the lubrication approximation, only valid for small surface gradients ($\partial_z h \ll 1$).

When the mean contact angle $\bar{\theta}$ is decreased, a strong increase of the viscous stress is observed but its localization remains mostly unchanged (see the Supplemental Material [12]). Another striking result is the influence of the defect height r_0: for contact angles close to the critical one, a reduction in size of the defect increases significantly the viscous stress but also affects its localization, which becomes concentrated closer from the contact line as r_0 is decreased (Fig. 2). This effect is not straightforward and may have important consequences on the wetting on surfaces with defects. Finally, the integration of the stress according to Eq. (5) leads to the normalized friction coefficient $\beta_{\mathrm{men}}/\eta$ as a function of $\bar{\theta}$, an example of which is plotted in Fig. 3 (dashed line). A significant increase of β_{men} is observed for decreasing contact angles in agreement with the experimental observations.

V. DISCUSSION

To quantitatively confront the FM-AFM experiments to the theoretical model, we use the force signal to determine the experimental contact angles $\bar{\theta}$. We assume that, due to the inhomogeneous thickness of the platinum rings, the meniscus depins from the defect for a contact angle θ_{break} larger than θ_{crit} value expected for an ideal defect. The maximum force before depinning then reads $F_{\mathrm{max}} = 2\pi\gamma(R + r_0)\cos\theta_{\mathrm{break}}$, which allows one to calculate the experimental contact angle for any d values using $\cos\bar{\theta} = (F/F_{\mathrm{max}})\cos\theta_{\mathrm{break}}$. The latter equation enables us to determine the contact angle for each d position without using the cantilever stiffness k only known within 20% error. For each experiment, we make a linear fit of the friction coefficient curve only taking into account the regions which are not influenced by the defects such as, for example, the portion between points (iv) and (v) in Fig. 1(b). The subtraction of this fit allows one to dispose of the viscous layer
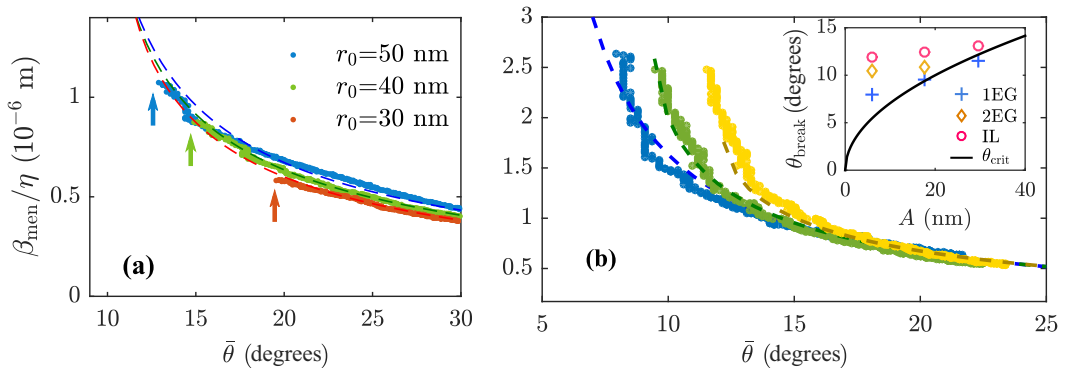
FIG. 4. Normalized friction coefficient β_{men}/η vs mean contact angle $\bar{\theta}$ for different operating conditions. The dashed lines are plots of the theoretical model [Eq. (5)]. (a) Influence of ring thickness r_0 on 2EG for $A = 6$ nm. The arrows indicate the value of θ_{break}. The values of the free parameters used are $\theta_{\text{break}} = 19.6°$, 15°, and 12.5° and $\beta_{\text{bottom}}/\eta R = 8.6$, 8.2, and 7 for $r_0 = 30$, 40, and 50 nm, respectively. (b) Influence of oscillation amplitude A for 1EG on a defect with $r_0 = 40$ nm: $A = 6$ nm, 17.7 nm, and 29.5 nm are plotted in blue, green, and yellow, respectively. The values of the free parameters used are $\theta_{\text{break}} = 7.9°$, 9.5°, and 11.5° and $\beta_{\text{bottom}}/\eta R = 0.13$, 0.89, and 2.7 for $A = 6$ nm, 17.7 nm, and 29.5 nm, respectively. Inset: plot of θ_{break} (symbols) and θ_{crit} (solid line) as a function of the oscillation amplitude for a defect of thickness $r_0 = 40$ nm. Symbol size corresponds to the error bar in θ_{break} measurements.

contribution on the side of the fiber, leaving only β_{men} and a constant term induced by the dissipation associated with the bottom of the tip, called β_{bottom}. The data are then fitted by computing the two free parameters β_{bottom} and θ_{break} which minimize the standard deviation between the experimental data and the theoretical curve [Eq. (5)]. The routine is performed with MATLAB, using the Curve Fitting toolbox. It (independently) determines the values of the adjusting parameters β_{bottom} and θ_{break} using the nonlinear least squares method. As for R and r_0, we use effective values measured by SEM. FM experiments were then performed over all the studied liquids. More than 90 experiments were carried out with two different home-made probes ($R = 80$ nm and 85 nm), defect thicknesses r_0 between 10 and 50 nm and oscillation amplitudes A ranging from 5 to 35 nm. Additionally, experiments were performed before and after surface cleaning by UV/O_3 treatment to assess the influence of tip wettability.

As an example, Fig. 3 displays six curves performed with three different liquids, before and after UV/O_3 treatment, on the same defect ($R = 85$ nm and $r_0 = 40$ nm) with an amplitude $A = 18$ nm. The agreement between the experimental data and the theoretical model is remarkable. A 10-fold enhancement of dissipation is observed when the contact angle is decreased from 50° to 10°. As expected, the 5 min surface cleaning does not affect the dissipation process since all curves superpose on a same master curve. Yet ozone cleaning has a strong impact on the θ_{break} values. The hydrophilic surfaces obtained after UV/O_3 treatment lead to a strong pinning which allows to reach smaller contact angle values. For example, for 1EG θ_{break} decreases from 18.5° to 9.5°, the latter value being very close to the value of $\theta_{\text{crit}} = 9.4°$. Consequently, the dissipation can reach larger values after ozone treatment. This is a common observation on all the measurements. When the tip is more hydrophobic, the liquid may detach between the dots forming the defect before the θ_{crit} value is reached. Note that, while the model is developed for small contact angles, confrontation with experiments demonstrates that it remains valid until $\theta_{\text{break}} \sim 50°$, values giving a weak dissipation. This is consistent with previous observations that the lubrication approximation yields good predictions for moderately large contact angles [2].

In order to discuss further the influence of the various parameters and the resulting values of the fitting variables θ_{break} and β_{bottom}, we report in Fi. 4(a) a comparison between the theoretical model and FM experiments performed on 3EG for (a) different defect thicknesses and (b) various
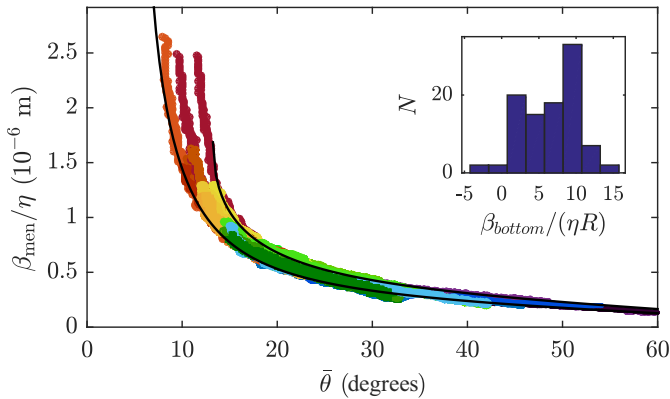
FIG. 5. Superposition of 30 experimental curves. In order to visualize different curves, the color is related to the θ_{break} value. The range of theoretical values is limited by two solid lines ($r_0 = 5$ nm, $A = 33$ nm for the higher one and $r_0 = 50$ nm, $A = 6$ nm for the lower one); Inset: Histogram of the β_{bottom} values extracted from the experimental data.

oscillation amplitudes. Figure 4(a) shows that the ring thickness r_0 has a low impact on the friction coefficient curve for 30 nm $\leqslant r_0 \leqslant$ 50 nm. Nevertheless, a systematic evolution of θ_{break} is observed: larger defect thicknesses lead to a stronger pinning of the defect, which results in a smaller θ_{break} value, as marked by the arrows on the curves. We also found that the oscillation amplitude plays a significant role only for contact angles close to θ_{crit}. Therefore its influence can be noticed only after the UV/O$_3$ treatment. The theoretical model reproduces well the influence of amplitude observed for contact angles smaller than 15° [see Fig. 4(b)]. A larger amplitude increases the value β_{men} at low $\bar{\theta}$ and also leads to an increase of the θ_{break} value, a general trend observed on all experiments.

These results show that the experimental conditions, namely, the defect size r_0, the oscillation amplitude A, and the surface wettability, have a small influence on the shape of the friction coefficient as a function of the contact angle. We therefore report in Fig. 5 30 curves obtained using different tips, defects, liquids, and amplitudes. All curves superimpose in a rather thin zone which is nicely bounded by the theoretical curves giving the extreme cases within the range of experimental conditions (10 nm $\leqslant r_0 \leqslant$ 50 nm and 6 nm $\leqslant$ A $\leqslant$ 33 nm). The highest dissipation is obtained for small defect and high amplitude ($r_0 = 5$ nm and $A = 33$ nm). From all the measurements (more than 90), we extracted values of the two adjustable parameters, namely, θ_{break} and β_{bottom}. The value of θ_{break} gives an indication of the pinning behavior. Strong pinning, which corresponds to low θ_{break} values, is reached for large defects on hydrophilic tips under weak forcing. This trend, consistent with macroscopic expectation, therefore remains valid down to nanometer-scale defects. In the optimal case, the θ_{crit} value expected for an ideal defect could be approached [see Fig. 4(c)]. Dynamic effects are also probably involved in the depinning transition since three liquids with similar surface tension and contact angle but varying viscosities show different pinning behaviors. This result, which has important consequences for the description of wetting dynamics on real surfaces, requires further investigations. Unlike θ_{break}, β_{bottom} does not show any systematic influence of amplitude, defect size, and wettability as expected from the model. Statistics over all experiments (see inset of Fig. 5) show that β_{bottom} is proportional to the liquid viscosity and is centered around a mean value $\beta_{\text{bottom}}/(\eta R) = 7$. This is consistent with expected values for a either a flat end or an hemispherical end leading to $\beta_{\text{bottom}} = 8\eta R$ [27] or $\beta_{\text{bottom}} = 3\pi \eta R$. This large dispersion comes from the fact that the tip end is ill-defined and moreover may evolve with time since measurements on hard surfaces are required, after each series of measurements, for calibration purposes. This hinders a more quantitative comparison with the theory.

VI. CONCLUSION

In conclusion, this work provides a comprehensive investigation of the viscous dissipation in anchored oscillating menisci. We find an excellent agreement between the experimental results and our lubrication-based theoretical model describing the flow pattern inside the oscillating meniscus. The confinement induced by the stretching of the meniscus leads to a strong increase of viscous stress which accounts for the surge of dissipated energy observed at a small angle. Note that this effect is amplified for small defect sizes, in which case the stress is strongly localized at the contact line with important consequences for the wetting dynamics on surfaces with defects. The fabrication of artificial nanometric defects also gives new insights on the depinning of the contact line which appears for a contact angle value θ_{break} larger than the theoretical one θ_{crit} obtained for a perfect pinning. The latter value could be approached using hydrophilic tips showing that the pinning is all the stronger that the oscillation amplitude A is small and the defect size r_0 is large. This study demonstrates that FM-AFM combined with the nanofabrication of dedicated probes with controlled defects is a unique tool for quantitative measurements of dissipation in confined liquids, down to the nanometer scale, and paves the way for a systematic study of open questions in wetting science regarding the extra dissipation which occurs when the contact line starts to move. In particular, our approach brings new insights for the role of surface defects, their pinning behavior, and the associated induced dissipation, down to the nanometer scale.

---

[1] P. G. de Gennes, Wetting: Statics and dynamics, Rev. Mod. Phys. **57**, 827 (1985).

[2] D. Bonn, J. Eggers, J. Indekeu, J. Meunier, and E. Rolley, Wetting and spreading, Rev. Mod. Phys. **81**, 739 (2009).

[3] J. H. Snoeijer and B. Andreotti, Moving contact lines: Scales, regimes, and dynamical transitions, Ann. Rev. Fluid Mech. **45**, 269 (2013).

[4] J. F. Joanny and P.-G. De Gennes, A model for contact angle hysteresis, J. Chem. Phys. **81**, 552 (1984).

[5] H. Perrin, R. Lhermerout, K. Davitt, E. Rolley, and B. Andreotti, Defects at the Nanoscale Impact Contact Line Motion at all Scales, Phys. Rev. Lett. **116**, 184502 (2016).

[6] X. Noblin, A. Buguin, and F. Brochard-Wyart, Vibrated sessile drops: Transition between pinned and mobile contact line oscillations, Eur. Phys. J. E **14**, 395 (2004).

[7] G. Michel, F. Pétrélis, and S. Fauve, Acoustic Measurement of Surface Wave Damping by a Meniscus, Phys. Rev. Lett. **116**, 174301 (2016).

[8] T. Fukuma, Water distribution at solid/liquid interfaces visualized by frequency modulation atomic force microscopy, Sci. Technol. Adv. Mater. **11**, 033003 (2010).

[9] A. Maali, T. Cohen-Bouhacina, and H. Kellay, Measurement of the slip length of water flow on graphite surface, Appl. Phys. Lett. **92**, 053101 (2008).

[10] J. Dupré de Baubigny, M. Benzaquen, C. Mortagne, C. Devailly, S. Kosgodagan Acharige, J. Laurent, A. Steinberger, J.-P. Salvetat, J.-P. Aimé, and T. Ondarçuhu, AFM study of hydrodynamics in boundary layers around micro- and nanofibers, Phys. Rev. Fluids **1**, 044104 (2016).

[11] S. Guo, M. Gao, X. Xiong, Y. J. Wang, X. Wang, P. Sheng, and P. Tong, Direct Measurement of Friction of a Fluctuating Contact Line, Phys. Rev. Lett. **111**, 026101 (2013).

[12] See Supplemental Material at http://link.aps.org/supplemental/10.1103/PhysRevFluids.2.102201 for tip fabrication, velocity profile and friction, and low patterns inside the meniscus.

[13] J. R. Vig, UV/ozone cleaning of surfaces, J. Vac. Sci. Technol. A **3**, 1027 (1985).

[14] H.-J. Butt and M. Jaschke, Calculation of thermal noise in atomic force microscopy, Nanotechnology **6**, 1 (1995).

[15] F. J. Giessibl, Advances in atomic force microscopy, Rev. Mod. Phys. **75**, 949 (2003).

[16] M. Delmas, M. Monthioux, and T. Ondarcuhu, Contact Angle Hysteresis at the Nanometer Scale, Phys. Rev. Lett. **106**, 136102 (2011).

[17] A. H. Barber, S. R. Cohen, and H. D. Wagner, Static and Dynamic Wetting Measurements of Single Carbon Nanotubes, Phys. Rev. Lett. **92**, 186103 (2004).

[18] M. M. Yazdanpanah, M. Hosseini, S. Pabba, S. M. Berry, V. V. Dobrokhotov, A. Safir, R. S. Keynton, and R. W. Cohn, Micro-Wilhelmy and related liquid property measurements using constant-diameter nanoneedle-tipped atomic force microscope probes, Langmuir **24**, 13753 (2008).

[19] J. Pérez, *Mécanique: fondements et applications: avec 300 exercices et problèmes résolus* (Dunod, Paris, 2001).

[20] The global capillary number can be evaluated to Ca $= A\omega\eta/\gamma \sim 10^{-3}$. However, this general criterion is not rigorously sufficient. It must be completed by its local counterpart (see the end of the theoretical model section for an *a posteriori* consistency check).

[21] B. V. Derjaguin, Theory of the distortion of a plane surface of a liquid by small objects and its application to the measurement of the contact angle of the wetting of thin filaments and fibres, Dokl. Akad. Nauk SSSR **51**, 517 (1946).

[22] D. F. James, The meniscus on the outside of a small circular cylinder, J. Fluid Mech. **63**, 657 (1974).

[23] J. Dupré de Baubigny, M. Benzaquen, L. Fabié, M. Delmas, J.-P. Aimé, M. Legros, and T. Ondarçuhu, Shape and effective spring constant of liquid interfaces probed at the nanometer scale: finite size effects, Langmuir **31**, 9790 (2015).

[24] E. Kirkinis and S. H. Davis, Hydrodynamic Theory of Liquid Slippage on a Solid Substrate Near a Moving Contact Line, Phys. Rev. Lett. **110**, 234503 (2013).

[25] P. A. Thompson and M. O. Robbins, Simulations of Contact-Line Motion: Slip and the Dynamic Contact Angle, Phys. Rev. Lett. **63**, 766 (1989).

[26] L. Bocquet and E. Charlaix, Nanofluidics, from bulk to interfaces, Chem. Soc. Rev. **39**, 1073 (2010).

[27] W. Zhang and H. A. Stone, Oscillatory motions of circular disks and nearly spherical particles in viscous flows, J. Fluid Mech. **367**, 329 (1998).

Supplemental material

Dynamics of an anchored oscillating nanomenisci

Caroline Mortagne, [1,2] Kévin Lippera,[1,3] Philippe Tordjeman,[2] Michael Benzaquen,[3] Thierry Ondarçuhu[1]

[1] Nanosciences group, CEMES-CNRS, 29 rue Jeanne Marvig,
31055 Toulouse Cedex 4 France

[2] IMFT - Université de Toulouse, CNRS-INPT-UPS, 1 allée du Professeur Camille Soula,
31400 Toulouse France

[3] LadHyX - Ecole Polytechnique, CNRS, Boulevard des Maréchaux,
91120 Palaiseau, France

SM1: Tip fabrication

A two-step process was developed to fabricate the non-conventional tips used in this study.

In a first step (Fig. S1), a nanofiber is milled from a conventional AFM tip (OLTESPA-R3, Bruker) using a dual beam FIB (1540 XB Cross Beam, Zeiss). The initial pyramidal tip is progressively cut by slices of 100 to 500 nm width in order to keep only the front edge of the pyramid. It results in a fiber with a rounded triangular profile. Note that, for the comparison between the experimental results and the theoretical model based on a cylindrical geometry, we use an effective theoretical radius which gives the same perimeter as the actual tip. Radius as small as 25 nm can be fabricated but, in this study, we used tips of 80 nm or 85 nm radius, which are large enough to accommodate enough defects.
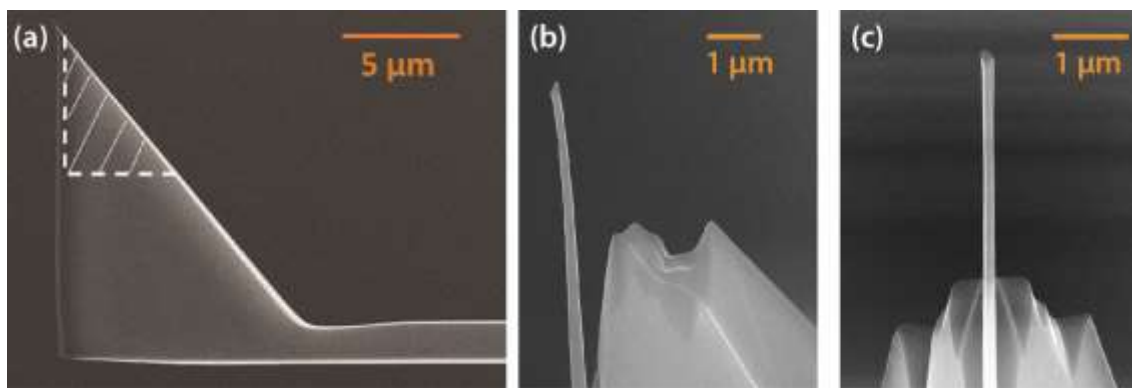

Figure S1: (a) Lateral SEM image of a OLTESPA-R3 (Bruker) tip. The hatched area represent the zone removed by FIB to carve the nanofiber; (b) – (c) Lateral and face view of a nanofiber after milling.

In a second step, defects are built on the nanofiber in order to pin the meniscus. This is achieved by Electron Beam Induced Deposition (EBID) using an ELPHY MultiBeam (Raith) and the gas injection system of the FIB. A platinum precursor gas injected close to the tip is decomposed by the electron beam, leaving platinum on the tip. Regular annular defects can not be achieved because a continuous motion of the electron beam results in a deposit which does not stick to the tip surface but rather forms a needle perpendicular to the tip. In order to solve

2

this issue, discontinuous defects are built, as shown in Figure S2. Spots with diameter ranging from 10 nm to 40 nm can be achieved. The distance between spots was adjusted in order to get the closest possible spots. Interestingly, due to the partial transparency of the thin nanofibers to electrons, thinner defects are also deposited on the back side of the tip. As a consequence of the annular defect inhomogeneity, the contact line can depin for a contact angle θ_{break} larger than the theoretical value θ_{crit}. Note that the defects rings form an angle of 11° with respect to the perpendicular to the tip axis in order to compensate for the inclination of the tip in the AFM head and insuring that the defect is perpendicular to the liquid interface.
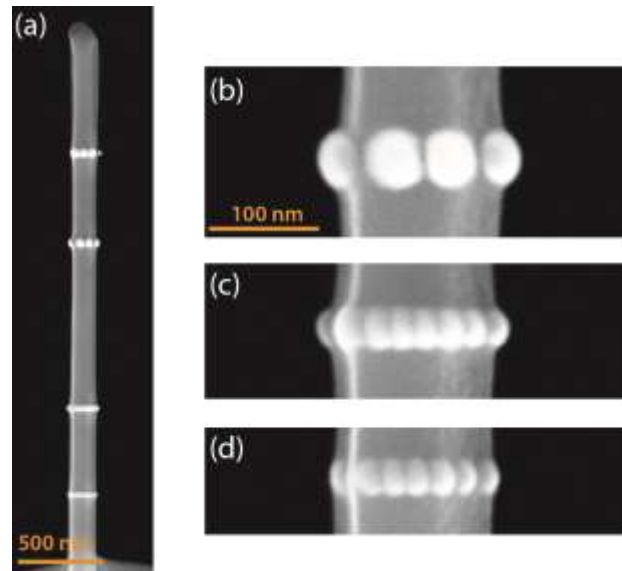

Figure S2: (a) SEM image of the same tip as in Fig. SM1 with 4 rings of defects deposited by EBID; (b) – (d) Zooms on the three lower defects.

SM2: Velocity profile and friction coefficient

We consider the flow induced by the interface motion of a liquid meniscus anchored on a cylinder rod, of radius R, oscillating along its axis, z. The meniscus contact line is pinned on an annular topographical defect of radius r_0. In the frame of reference attached to the cylinder, the velocity field is solution, for a purely viscous Newtonian liquid under the lubrication approximation, of the Stokes equation

$$\partial_z P = \eta \Delta_r v, \tag{SI1}$$

where P is the hydrodynamic pressure, η is the fluid viscosity and v is the velocity component in the z direction. Equation (SI1), together with a no-slip boundary condition at the rod's surface, at $r = R$, and a no-stress boundary condition at the free interface, at $r = h(z)$, relates the velocity field to the hydrodynamic pressure gradient through the equation:

$$v(r,z) = \frac{\partial_z P(z) \left(r^2 - 2h^2(z) \ln\left(\frac{r}{R}\right) - R^2 \right)}{4\,\eta}. \tag{SI2}$$

Furthermore, the velocity field is related to the interface profile through the mass conservation equation

$$\partial_t (\pi h^2) + 2\pi \partial_z \int_R^{h(z)} dr\, v(r,z)\, r = 0. \tag{SI3}$$

From Eq. (SI3) we derive the pressure gradient inside the meniscus

$$\partial_z P(z) = -\frac{8\eta \int_0^z du\, \partial_t(h^2)}{R^4 + 3h^4 - 4h^2 R^2 - 4h^4 \ln\left(\frac{h}{R}\right)}, \tag{SI4}$$

which, in turns, gives the velocity profile as a function of the interface profile

$$v(r,z) = \frac{2 \left(R^2 + 2h^2 \ln\left(\frac{r}{R}\right) - r^2 \right) \int_0^z du\, \partial_t(h^2)}{R^4 + 3h^4 - 4h^2 R^2 - 4h^4 \ln\left(\frac{h}{R}\right)}. \tag{SI5}$$

Since the capillary number is small ($Ca = A\,\omega\eta/\gamma \sim 10^{-3}$) we assume that viscous effects do not affect the shape of the liquid interface. The meniscus profile is therefore solution of the Laplace equation resulting from the balance between capillary and hydrostatic pressures, which yields the well-known catenary shape

$$h(z) = (R + r_0)\cos\theta \cosh\left(\frac{z}{(R + r_0)\cos(\theta)} - \ln\left[\frac{\cos(\theta)}{1 + \sin(\theta)}\right]\right), \qquad \text{(SI6)}$$

where θ is the wetting contact angle of the meniscus.

As the contact line is pinned during the rod oscillation, the meniscus height, $Z_0(\theta)$, oscillates around its mean position, $Z_0(\bar{\theta})$, with $Z_0(\theta[t]) = Z_0(\bar{\theta}) + A\cos(\omega t)$, where $\bar{\theta}, A$ and ω are respectively the mean contact angle, the amplitude and the angular frequency of the oscillation. Together with the expression of $Z_0(\theta)$, which reads for small contact angle

$$Z_0(\theta) = (R + r_0)\cos\theta \left[\ln\left(\frac{4l_c}{R+r_0}\right) - \gamma_E\right], \qquad \text{(SI7)}$$

we derive thus the temporal evolution of the contact angle

$$\cos\theta = \cos\bar{\theta} + \frac{A\cos(\omega t)}{(R + r_0)\left[\ln\left(\frac{4l_c}{R + r_0}\right) - \gamma_E\right]}. \qquad \text{(SI8)}$$

Hence, Eqs. (SI5), (SI6) and (SI8) give the velocity profile inside the meniscus. Note that our model is meant to deal with positive contact angles only, even if the defect thickness could in principle allow slightly negative ones. From Eq. (SI8) we obtain therefore a critical contact angle, θ_{crit}, corresponding to the minimum value of $\bar{\theta}$ allowed by the model, with

$$\cos\theta_{crit} = 1 - \frac{A}{(R + r_0)\left[\ln\left(\frac{4l_c}{R + r_0}\right) - \gamma_E\right]}. \qquad \text{(SI9)}$$

We can now determinate the friction coefficient associated with the meniscus, β_{men}. For a forced harmonic oscillator that dissipates energy through viscous damping, the mean energy loss during an oscillation cycle, P, is related to the friction coefficient through the relation

$$P = \frac{\beta_{men}\,(A\omega)^2}{2}. \tag{SI10}$$

Furthermore, P is given, for a viscous Newtonian liquid under lubrication approximation, by

$$P = \left\langle \eta \oint_V (\partial_r v)^2 \, dV \right\rangle_t, \tag{SI11}$$

where $\langle\ \ \rangle_t$ designates the temporal average over an oscillation cycle. Combining Eqs. (SI10) and (SI11) we obtain

$$\beta_{mean} = \left\langle \frac{2\eta}{(A\omega)^2} \oint_V (\partial_r v)^2 \, dV \right\rangle_t. \tag{SI12}$$

The case of small amplitude

We consider the asymptotic limit of small oscillation amplitude where $\sin\theta(t) \simeq \sin\bar{\theta}$ and $h(\theta(t)) \simeq h(\bar{\theta})$. Under this approximation, the derivative of the contact angle $\dot{\theta}$ reads

$$\dot{\theta}(t) \simeq \frac{A\,\omega\sin(\omega t)}{\sin\bar{\theta}(R + r_0)\left[\ln\left(\frac{4l_c}{R+r_0}\right) - \gamma_E\right]}, \tag{SI13}$$

and the normalized viscous stress is given by the equation

$$\partial_r v \simeq \frac{4\dot{\theta}(h^2/r - r)\int_0^{h(z)} du\,\partial_{\bar{\theta}}(h^2)}{R^4 + 3h^4 - 4h^2 R^2 - 4h^4 \ln\left(\frac{h}{R}\right)} = A\,\tilde{\sigma}_{rz}, \tag{SI14}$$

where we introduce $\tilde{\sigma}_{rz}(r, z, \bar{\theta}) = \dfrac{4\omega\sin(\omega t)\left(\frac{h^2}{r} - r\right)\int_0^{h(z)} du\,\partial_{\bar{\theta}}(h^2)}{\sin\bar{\theta}(R+r_0)\left[\ln\left(\frac{4l_c}{R+r_0}\right) - \gamma_E\right]\left(R^4 + 3h^2 - 4h^2 R^2 - 4h^4\ln\left(\frac{h}{R}\right)\right)}$. Since $\partial_r v$

is proportional to the amplitude A, we obtain from Eq. (SI12) that β_{mean} does not depend on A in the asymptotic case of small amplitude. However, the Taylor expansion of Eq. (SI9) shows that the critical contact angle , θ_{crit}, varies as the square root of A with

$$\theta_{crit} = \sqrt{\frac{2A}{(R + r_0)\left[\ln\left(\frac{4l_c}{R+r_0}\right) - \gamma_E\right]}}. \tag{SI15}$$

SM3: Flow patterns inside the meniscus: influence of the mean contact angle $\bar{\theta}$

The hydrodynamic model described in the paper provides a comprehensive description of flow patterns in an oscillating nanomeniscus which lead to the measured friction coefficient. In Fig. S3 are reported the viscous stress field inside the meniscus as the mean contact angle $\bar{\theta}$ is reduced from $\bar{\theta} = 22°$ down to $\bar{\theta} = \theta_{crit} = 6.73°$ which is the depinning contact angle associated with the conditions used in the calculation, namely $r_0 = 40$ nm and $A = 10$ nm. The maximum stress is obtained at the fiber surface at a distance of about $2.5\,r_0$ from the contact line. The decrease of contact angle significantly increases the value of the stress without any noticeable modification of the position of its localization inside the nanomeniscus.
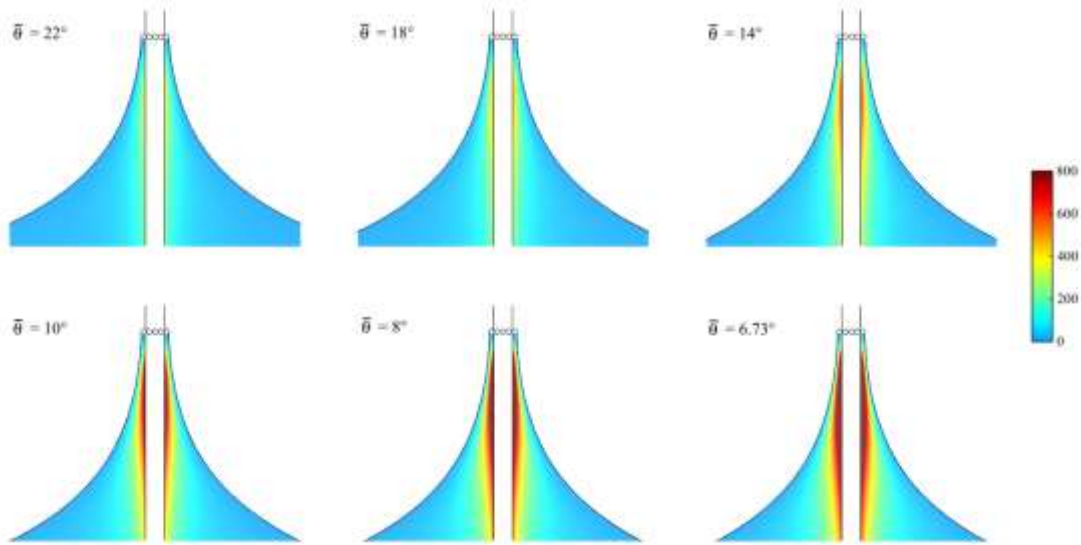

Figure S3: Viscous stress field $\eta\partial_r v$ (color gradient), computed at t = 0, for 6 different contact angles and $R = 100\ nm, r_0 = 30\ nm,\ l_c = 2\ mm, A = 10\ nm, f = 65\ kHz$ and $\eta = 30\ mPa.s$. Color bar in Pa.